

1908 **Chapter 9**  
1909 **Weak Focusing Synchrotron**

1910 **Abstract** This Chapter introduces to the weak focusing synchrotron, and to the the-  
1911 oretical material needed for the simulation exercises. It begins with a brief reminder  
1912 of the historical context, and continues with beam optics and acceleration techniques  
1913 which the weak synchrotron principle and methods lean on. Regarding the latter, it  
1914 relies on basic charged particle optics and acceleration concepts introduced in the  
1915 previous Chapters, and further addresses the following aspects:

- 1916 - fixed closed orbit,
- 1917 - periodic structure,
- 1918 - periodic motion stability,
- 1919 - optical functions,
- 1920 - synchrotron motion,
- 1921 - depolarizing resonances.

1922 The simulation of weak synchrotrons only require a very limited number of optical  
1923 elements; actually two are enough: DIPOLE or BEND to simulate combined function  
1924 dipoles, and DRIFT to simulate straight section. A third one CAVITE, is required  
1925 for acceleration. Particle monitoring requires keywords introduced in the previous  
1926 Chapters, including FAISCEAU, FAISTORE, possibly PICKUPS, and some others.  
1927 Spin motion computation and monitoring resort to SPNTRK, SPNPRT, FAISTORE.  
1928 Optics matching and optimization use FIT[2]. SYSTEM again is used to shorten the  
1929 input data files.

1930 **Notations used in the Text**

$B; \mathbf{B}, B_{x,y,s}$	field value; field vector, its components in the moving frame
$B\rho = p/q; B\rho_0$	particle rigidity; reference rigidity
$C; C_0$	orbit length, $C = 2\pi R + \left[ \begin{array}{l} \text{straight} \\ \text{sections} \end{array} \right]$ ; reference, $C_0 = C(p = p_0)$
$E$	particle energy
EFB	Effective Field Boundary
$f_{\text{rev}}, f_{\text{rf}}$	revolution and accelerating voltage frequencies
$h$	RF harmonic number, $h = f_{\text{rf}}/f_{\text{rev}}$
$m; m_0; M$	mass, $m = \gamma m_0$ ; rest mass; in units of MeV/c <sup>2</sup>
$n = \frac{\rho}{B} \frac{dB}{d\rho}$	focusing index
$\mathbf{p}; p; p_0$	momentum vector; its modulus; reference
$P_i, P_f$	polarization, initial, final
$q$	particle charge
$r, R$	orbital radius; average radius, $R = C/2\pi$
$s$	path variable
$v$	particle velocity
$V(t); \hat{V}$	oscillating voltage; its peak value
$x, x', y, y'$	horizontal and vertical coordinates in the moving frame
1931 $\alpha$	momentum compaction
$\alpha$	trajectory angle
$\beta = v/c; \beta_0; \beta_s$	normalized particle velocity; reference; synchronous
$\beta_u$	betatron functions ( $u : x, y, Y, Z$ )
$\gamma = E/m_0$	Lorentz relativistic factor
$\delta p$	momentum offset or Dirac distribution
$\Delta p$	momentum offset
$\varepsilon$	wedge angle
$\varepsilon_u$	Courant-Snyder invariant ( $u : x, r, y, l, Y, Z, s$ , etc.)
$\epsilon_R$	strength of a depolarizing resonance
$\mu_u$	betatron phase advance, $\mu_u = \int_{\text{period}} ds/\beta_u(s)$ ( $u : x, y, Y, Z$ )
$\nu_u$	wave number or “tune”, radial, vertical, synchrotron ( $u : x, y, Y, Z, l$ )
$\rho, \rho_0$	curvature radius; reference
$\sigma$	beam matrix
$\phi; \phi_s$	particle phase at voltage gap; synchronous phase
$\phi_u$	betatron phase advance, $\phi_u = \int ds/\beta_u$ ( $u : x, y, Y, \text{ or } Z$ )
$\varphi$	spin angle to the vertical axis

1932 **Introduction**

1933 The synchrotron is an outcome of the mid-1940s longitudinal phase focusing syn-  
 1934 chronous acceleration concept [1, 2]. In its early version, transverse beam stability

1935 in the synchrotron during the thousands of turns that the acceleration lasts was based  
 1936 on the technique known at the time: weak focusing, as in the cyclotron and in the be-  
 1937 tatron. An existing betatron was used to first demonstrate phase-stable synchronous  
 1938 acceleration with slow variation of the magnetic field, on a fixed orbit, in 1946 [3],  
 1939 - closely following the demonstration of the principle of phase focusing using a  
 1940 fixed-field cyclotron [4].

1941 Phase focusing states that stability of the longitudinal motion, longitudinal focus-  
 1942 ing, is obtained if particles in a bunch, which have a natural energy spread, arrive  
 1943 at the accelerating gap in the vicinity of a proper phase of the oscillating voltage,  
 1944 the synchronous phase; if this condition is fulfilled the bunch stays together, in the  
 1945 vicinity of the latter, during acceleration. Synchrotrons operate in general in a non-  
 1946 isochronous regime: the revolution period changes with energy; as a consequence,  
 1947 in order to maintain an accelerated bunch on the synchronous phase, the RF voltage  
 1948 frequency, which satisfies  $f_{rf} = hf_{rev}$ , has to change continuously from injection to  
 1949 top energy. The reference orbit in a synchrotron is maintained at constant radius by  
 1950 ramping the guiding field in the main dipoles in synchronism with the acceleration,  
 1951 as in the betatron [5].

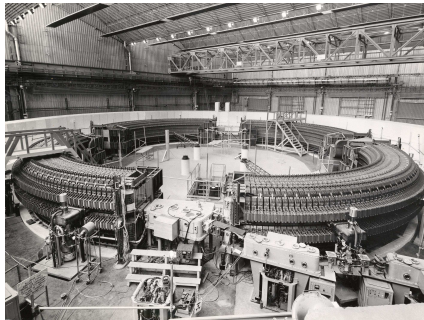


**Fig. 9.1** SATURNE I at Saclay [6], a 3 GeV, 4-period, 68.9 m circumference, weak focusing synchrotron, constructed in 1956-58. The injection line can be seen in the foreground, injection is from a 3.6 MeV Van de Graaff (not visible)

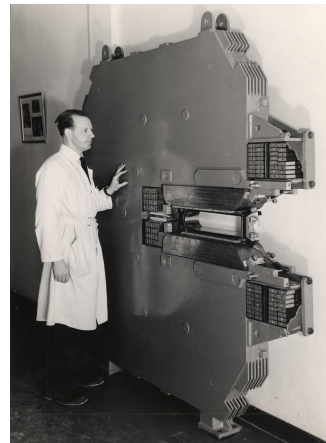


**Fig. 9.2** A slice of SATURNE I dipole [6]. The slight gap tapering is hardly visible (increasing outward), it determines the weak index condition  $0 < n < 1$

1952 The synchrotron concept allowed the highest energy reach by particle accelerators  
 1953 at the time, it led to the construction of a series of proton rings with increasing  
 1954 energy [7]: 1 GeV at Birmingham (1953), 3.3 GeV at the Cosmotron (Brookhaven  
 1955 National Laboratory, 1953-1969), 6.2 GeV at the Bevatron (Berkeley, 1954-1993),  
 1956 10 GeV at the Synchro-Phasotron (JINR, Dubna, 1957-2003), and a few additional  
 1957 ones in the late 1950s well into the era of the concept which would essentially  
 1958 dethrone the weak focusing method and its quite bulky rings of magnets which were

1959 a practical limit to further increase in energy<sup>1</sup>: the strong focusing synchrotron (the  
 1960 object of Chapter 10). The general layout of these first weak focusing synchrotrons  
 1961 included straight sections (often 4, Fig. 9.1), which allowed insertion of injection  
 1962 (Fig. 9.1) and extraction systems, accelerating cavities, orbit correction and beam  
 1963 monitoring equipment.

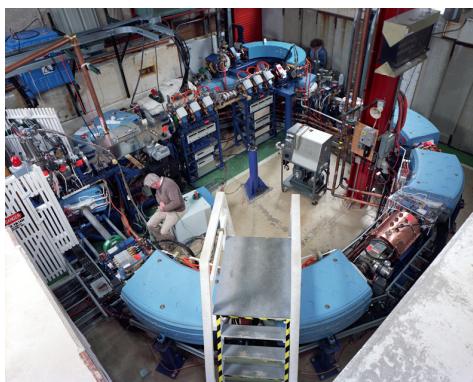


**Fig. 9.3** Left: Loma Linda University medical synchrotron [8], during commissioning in 1989 at the Fermilab National Laboratory where it was designed

1964 The next decades following the invention of the synchrotron saw applications in  
 1965 many fields of science including fixed-target nuclear physics for particle discovery,  
 1966 material science, medicine, industry. Its technological simplicity still makes it an  
 1967 appropriate technology today in low energy beam application when relatively low  
 1968 current is not a concern, as in the hadrontherapy application (Fig. 9.3) [9, 10]: it  
 1969 essentially requires a single type of a simple dipole magnet, an accelerating gap, some  
 1970 command-control instrumentation, whereas it procures greater beam manipulation  
 1971 flexibilities compared to (synchro-)cyclotrons.

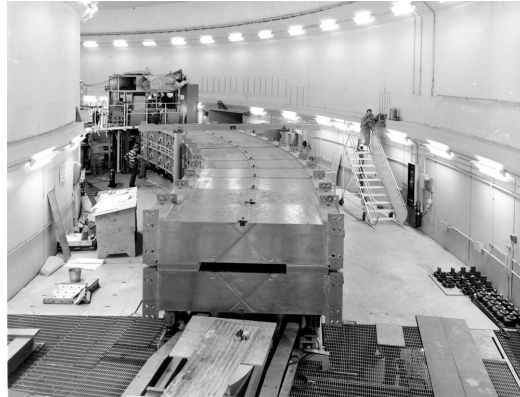
### 1972 *Polarized beams*

1973 The availability of polarized proton sources allowed the acceleration of polarized  
 1974 beams to high energy. The possibility was considered from the early times at Argonne  
 1975 ZGS (Zero-Gradient Synchrotron), a 12 GeV weak focusing synchrotron operated  
 1976 over 1964-1979 [11] (Fig. 9.4). Up to 70% polarization transmission through the syn-  
 1977 chrotron was achieved, for the first time in a synchrotron<sup>2</sup> and reaching multi-GeV  
 1978 energy in 1973, up to 17.5 GeV/c with *appreciable polarizations* [12]. Polariza-  
 1979 tion preservation techniques included harmonic orbit correction and fast betatron  
 1980 tune jump at strongest depolarizing resonances [13] (Fig. 9.16). Experiments were  
 1981 performed to assess the possibility of polarization transmission in strong focusing

<sup>1</sup> The story has it that it is possible to ride a bicycle in the vacuum chamber of Dubna's Synchro-Phasotron.

<sup>2</sup> Polarized beam had been accelerated in cyclotrons, at earlier times.

**Fig. 9.4** The ZGS at Argonne during construction. A 12 GeV, 8-dipole, 4-period, 172 m circumference, wedge focusing synchrotron. The two persons inside and outside the ring, in the background, give an idea of the size of the magnets



1982 synchrotrons, and polarization lifetime in colliders [14]. Acceleration of polarized  
1983 deuteron was achieved in the late 1970s, when sources were made available [15].

## 1984 9.1 Basic Concepts and Formulae

1985 The synchrotron is based on two key principles. On the one hand, a slowly varying  
1986 magnetic field to maintain a constant orbit during acceleration,

$$B(t) \times \rho = p(t)/q, \quad \rho = \text{constant}, \quad (9.1)$$

1987 with  $p(t)$  the particle momentum and  $\rho$  the bending radius in the dipoles. On the other  
1988 hand, on synchronous acceleration for longitudinal phase stability. In a regime where  
1989 the velocity change with energy cannot be ignored (non-ultrarelativistic particles),  
1990 the latter requires a modulation of the accelerating voltage frequency so to satisfy

$$f_{rf}(t) = h f_{rev}(t) \quad (9.2)$$

1991 Synchronism between accelerating voltage oscillation and the revolution motion  
1992 keeps the bunch on the synchronous phase at traversal of the accelerating gaps.  
1993 Synchronous acceleration is technologically simpler in the case of electrons, as  
1994 frequency modulation is unnecessary beyond a few MeV; for instance, from  $v/c =$   
1995  $0.9987$  at 10 MeV to  $v/c \rightarrow 1$  the relative change in revolution frequency amounts  
1996 to  $\delta f_{rev}/f_{rev} = \delta\beta/\beta < 0.0013$ .

1997 These are two major evolutions compared to the cyclotron, where, instead, the  
1998 magnetic field is fixed - the reference orbit spirals out, and, by virtue of the isochro-  
1999 nism of the orbits, the oscillating voltage frequency is fixed as well.

2000 A fixed orbit reduces the radial extent of individual guiding magnets, allowing a  
2001 ring structure comprised of a circular string of dipoles. For the sake of comparison:  
2002 a synchrocyclotron instead uses a single, massive dipole; increased energy requires

2003 increased radial extent of the magnet to allow for the greater bending field integral  
 2004 (*i.e.*,  $\oint B dl = 2\pi R_{\max} \hat{B} = p_{\max}/q$ ), thus a volume of iron increasing more than  
 2005 quadratically with bunch rigidity.

2006 One or the other of the weak index ( $-1 < k < 0$ , Sect. 4.2.2) and/or wedge  
 2007 focusing (Sect. 15.3.1) are used in weak focusing synchrotrons. Transverse stability  
 2008 was based on the latter at Argonne ZGS (Zero-Gradient Synchrotron: the main  
 2009 magnet had no field index); ZGS accelerated polarized proton beams, weak focusing  
 2010 resulted in weak depolarizing resonances, an advantage in that matter [14].

2011 Due to the necessary ramping of the field, and of the RF frequency to follow,  
 2012 in order to maintain a constant orbit, the synchrotron is a pulsed accelerator, the  
 2013 acceleration is cycled, from injection to top energy, repeatedly. The repetition rate  
 2014 of the acceleration cycle depends on the type of power supply. If the ramping uses a  
 2015 constant electromotive force ( $E=V+ZI$  is constant), then

$$B(t) \propto (1 - e^{-\frac{t}{\tau}}) = 1 - \left[ 1 - \left(\frac{t}{\tau}\right) + \left(\frac{t}{\tau}\right)^2 - \dots \right] \approx \frac{t}{\tau} \quad (9.3)$$

2016 essentially linear;  $\dot{B} = dB/dt$  does not exceed a few Tesla/second: the repetition rate  
 2017 of the acceleration cycle if of the order of a Hertz. If instead the magnet winding  
 2018 is part of a resonant circuit then the field oscillates from an injection threshold to a  
 2019 maximum value,  $B(t) : B_0 \rightarrow B_0 + \hat{B}$ , as in the betatron; the repetition rate is up to  
 2020 a few tens of Hertz. In both cases anyway B imposes its law and the other quantities  
 2021 comprising the acceleration cycle (RF frequency in particular) will follow B(t).

2022 For the sake of comparison: in a synchrocyclotron the field is constant, thus  
 2023 acceleration can be cycled as fast as the swing of the voltage frequency allows  
 2024 (hundreds of Hz are common practice); assume a conservative 10 kVolts per turn,  
 2025 thus of the order of 10,000 turns to 100 MeV, with velocity  $0.046 < v/c < 0.43$   
 2026 from 1 to 100 MeV, proton. Take  $v \approx 0.5c$  to make it simple, an orbit circumference  
 2027 below 30 meter, thus the acceleration takes of the order of  $10^4 \times C/0.5c \approx \text{ms}$  range,  
 2028 potentially a repetition rate in kHz range, more than an order of magnitude beyond  
 2029 the reach of a rapid-cycling pulsed synchrotron.

### 2030 9.1.1 Periodic Stability

2031 This section introduces the various components of the transverse focusing and the  
 2032 conditions for periodic stability in a weak focusing synchrotron. It builds on material  
 2033 introduced in Chap. 4, Classical Cyclotron.

#### 2034 9.1.1.1 Closed orbit

2035 The concept is found in the betatron, which accelerates particles on a constant orbit  
 2036 (Chap. 7). The closed orbit is fixed, and maintained during acceleration by ensuring

2037 that the relationship Eq. 9.1 is satisfied. In a perfect ring, the closed orbit is along an  
 2038 arc in the bending magnets and straight along the drifts, Fig. 9.5.

2039 Particle motion is defined in a moving frame (O;s,x,y) whose origin coincides  
 2040 with the location of an ideal particle following the reference orbit. The moving frame  
 2041  $s$  axis is tangent to the reference orbit, its transverse horizontal axis  $x$  is normal to  
 2042 the  $s$  axis, its vertical axis  $y$  is normal to the  $(s, x)$  plane (Fig. 4.8, Sect. 4.2.2).

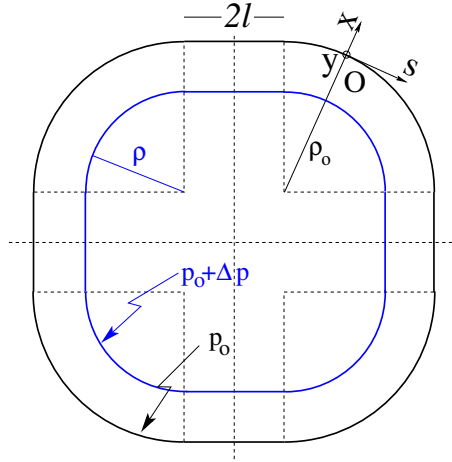


**Fig. 9.5** A  $2\pi/4$  axially symmetric structure with four drift spaces. Orbit length on reference momentum  $p_0$  is  $C = 2\pi\rho_0 + 8l$ . (O;s,x,y) is the moving frame, along the reference orbit. The orbit for momentum  $p = p_0 + \Delta p$  ( $\Delta p < 0$ , here) is at constant distance  $\Delta x = \frac{\rho_0}{1-n} \frac{\Delta p}{p_0} = \frac{R}{(1+k)(1-n)} \frac{\Delta p}{p_0}$  from the reference orbit

2043 **9.1.1.2 Transverse Focusing**

2044 Radial motion stability around a reference closed orbit in an axially symmetric dipole  
 2045 field requires a field index (Sect. 4.2.2),

$$n = -\frac{\rho_0}{B_0} \left. \frac{\partial B_y}{\partial x} \right|_{x=0, y=0} \quad (9.4)$$

2046 a quantity evaluated on the reference arc in the dipoles, satisfying the weak focusing  
 2047 condition (Eq. 4.11 with  $n = -k$ )

$$0 < n < 1 \quad (9.5)$$

2048 This condition can be obtained with a tapered gap (as in SATURNE dipoles, Fig. 9.2)  
 2049 causing the magnetic field to decrease slowly with radius, so resulting in both axial  
 2050 and radial focusing (Figs. 9.6, 9.7). Note the sign convention here, the cyclotron uses  
 2051 the opposite sign (Eq. 4.10). This condition holds regardless of the presence of drifts  
 2052 or not. Adding drift spaces between the dipoles, the reference orbit is comprised of  
 2053 arcs of radius  $\rho_0$  in the magnets, and straight segments along the drift spaces that  
 2054 connect these arcs. This requires defining two radii, namely,

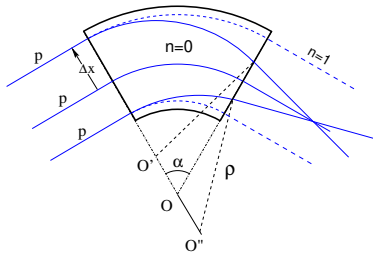


**Fig. 9.6** Geometrical focusing: in a sector dipole with focusing index  $n = 0$ , parallel incoming rays of equal momenta experience the same curvature radius  $\rho$ , their trajectories converge as outer trajectories have a longer path in the field, inner ones shorter. An index value  $n=1$  cancels that effect: parallel incoming rays exit parallel

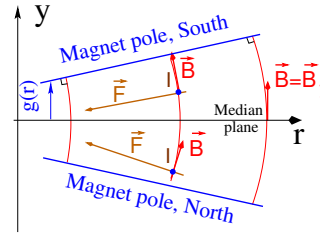


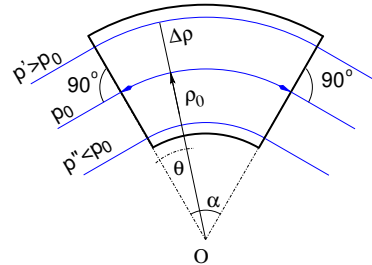
**Fig. 9.7** Axial motion stability requires proper shaping of field lines:  $B_y$  has to decrease with radius. The Laplace force pulls a positive charge with velocity pointing out of the page, at I, toward the median plane. Increasing the field gradient ( $n$  closer to 1, gap opening up faster) increases the focusing

- 2055 (i) the magnet curvature radius  $\rho_0$ ,  
 2056 (ii) an average radius  $R = C/2\pi = \rho_0 + Nl/\pi$  (with  $C$  the length of the reference  
 2057 closed orbit and  $2l$  the drift length) (Fig. 9.5) which also writes

$$R = \rho_0(1 + k), \quad k = \frac{Nl}{\pi\rho_0} \quad (9.6)$$

2058 Adding drift spaces decreases the average focusing around the ring.

**Fig. 9.8** In a sector dipole with radial index  $n \neq 0$ , closed orbits follow arcs of constant field. A closed orbit at  $p_0 + \Delta p$  follows an arc of radius  $\rho_0 + \Delta\rho$ ,  $\Delta\rho = \Delta p / (1 + n)qB_0$



### 2059 Geometrical focusing

2060 The limit  $n \rightarrow 1$  of the transverse motion stability domain corresponds to a cancel-  
 2061 lation of the geometrical focusing (Fig. 9.6): in a constant field dipole (radial field  
 2062 index  $n=0$ ) the longer (respectively shorter) path in the magnetic field for parallel  
 2063 trajectories entering the magnet at greater (respectively smaller) radius result in  
 2064 convergence. This effect is cancelled, *i.e.*, trajectory angle is the same whatever the



2065 entrance radius, if the curvature center is made independent of the entrance radius:  
 2066  $OO' = 0, O''O = 0$ . This occurs if trajectories at an outer (inner) radius experience a  
 2067 smaller (greater) field such as to satisfy  $BL = B\rho\alpha = C^{st}$ . Differentiating  $B\rho = C^{st}$   
 2068 gives  $\frac{\Delta B}{B} + \frac{\Delta\rho}{\rho} = 0$ , with  $\Delta\rho = \Delta x$ , so yielding  $n = -\frac{\rho_0}{B_0} \frac{\Delta B}{\Delta x} = 1$ . The focal distance  
 2069 associated with the curvature is (Eq. 4.12 with  $R = \rho_0$ )  $f = \frac{\rho_0^2}{L}$ . Optical drawbacks  
 2070 of the weak focusing method include the weakness of the focusing and the absence  
 2071 of independent radial and axial focusing.

2072 *Wedge Focusing*

2073 Entrance and exit wedge angles may be used to ensure transverse focusing, Fig. 9.9:  
 2074 opening the magnetic sector increases the horizontal focusing (and decreases the  
 2075 vertical focusing); closing the magnetic sector has the reverse effect (see Sect. 15.3.1).

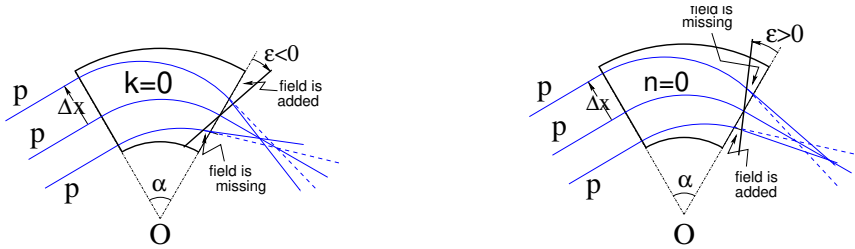


**Fig. 9.9** Left: a focusing wedge ( $\epsilon < 0$ ); opening the sector increases horizontal focusing and decreases vertical focusing. Right: a defocusing wedge ( $\epsilon > 0$ ), closing the sector, has the reverse effect. This is the origin of the focusing in the ZGS zero-gradient dipoles

2076 In a point transform approximation, at the wedge the trajectory undergoes a local  
 2077 deviation proportional to the distance to the optical axis, amounting to

$$\Delta x' = \frac{\tan \epsilon}{\rho_0} \Delta x, \quad \Delta y' = -\frac{\tan(\epsilon - \psi)}{\rho_0} \Delta y \quad (9.7)$$

2078 The  $\psi$  angle component is a correction for the fringe field extent (Eq. 15.21); the  
 2079 effect of the latter, of the first order on the vertical focusing, is of second order  
 2080 horizontally.

2081 Profiling the magnet gap in order to adjust the focal distance complicates the  
 2082 magnet; a parallel gap,  $n = 0$ , makes it simpler, for that reason edge focusing may  
 2083 be preferred. Wedge vertical focusing in the ZGS ( $\epsilon > 0$ ) was at the expense of  
 2084 horizontal geometrical focusing (Fig. 9.6). This was an advantage though, for the  
 2085 acceleration of polarized beams, as radial field components (which are responsible for  
 2086 depolarization) were only met at the EFBs of the eight main dipoles, and weak [12].  
 2087 Preserving beam polarization at high energy required tight control of the tunes, this

2088 was achieved by pole face windings added at the ends of the dipoles [17, 18], pulsed  
2089 to control the amplitude detuning, resulting in a control of the tunes at 0.01 level.

### 2090 9.1.1.3 Betatron motion

2091 The first order differential equations of motion in the moving frame (Fig. 9.5) derive  
2092 from the Lorentz equation

$$\frac{d\mathbf{m}\mathbf{v}}{dt} = q\mathbf{v} \times \mathbf{B} \Rightarrow m \frac{d}{dt} \begin{Bmatrix} \frac{ds}{dt} \mathbf{s} \\ \frac{dx}{dt} \mathbf{x} \\ \frac{dy}{dt} \mathbf{y} \end{Bmatrix} = q \begin{Bmatrix} \left( \frac{dx}{dt} B_y - \frac{dy}{dt} B_x \right) \mathbf{s} \\ -\frac{ds}{dt} B_y \mathbf{x} \\ \frac{ds}{dt} B_x \mathbf{y} \end{Bmatrix} \quad (9.8)$$

2093 Motion in a weak index dipole field is solved in Sect. 4.2.2, Classical Cyclotron: in  
2094 the latter substitute  $\rho$  to  $R$ ,  $n = -\frac{\rho_0}{B_0} \frac{\partial B_y}{\partial x}$  to  $-k$ , evaluated on the reference orbit.  
2095 Taylor expansions of the transverse field components in the moving frame (Eq. 4.6)  
2096 lead to

$$\begin{aligned} B_y(\rho)|_{y=0} &= B_0(1 - n \frac{x}{\rho_0}) + \mathcal{O}(x^2) \\ B_x(0+y) &= -n \frac{B_0}{\rho_0} y + \mathcal{O}(y^3) \end{aligned} \quad (9.9)$$

2097 Assume transverse stability:  $0 < n < 1$ ; in the approximation  $ds \approx vdt$  (Eq. 4.13)  
2098 Eqs. 9.8, 9.9 lead to the differential equations of motion

$$\frac{d^2x}{ds^2} + \frac{1-n}{\rho_0^2} x = 0, \quad \frac{d^2y}{ds^2} + \frac{n}{\rho_0^2} y = 0 \quad (9.10)$$

2099 It results that, in an S-periodic structure comprised of gradient dipoles, wedges  
2100 and drift spaces, the differential equation of motion takes the general form of Hill's  
2101 equation, a second order differential equation with periodic coefficient, namely (with  
2102  $u$  standing for  $x$  or  $y$ ),

$$\begin{cases} \frac{d^2u}{ds^2} + K_u(s)u = 0 \\ K_u(s+S) = K_u(s) \end{cases} \quad \text{with} \quad \begin{cases} \text{in dipoles : } \begin{cases} K_x = \frac{1-n}{\rho_0^2} \\ K_y = \frac{n}{\rho_0^2} \end{cases} \\ \text{at a wedge at } s = s_0 : K_x = \frac{\pm \tan \varepsilon}{\rho_0} \delta(s - s_0) \\ \text{in drift spaces : } \frac{1}{\rho_0} = 0, K_x = K_y = 0 \end{cases} \quad (9.11)$$

2103  $K_u(s)$  is S-periodic,  $S = 2\pi R/N$  ( $S = C/4$  for instance in a 4-periodic ring,  
2104 Figs. 9.1, 9.5).

2105 The solution of Eqs. 9.11 is not as straightforward as in the cyclotron where  $K_u$  is  
2106 constant around the ring (Eq. 4.14), which results in a sinusoidal motion (Eq. 4.16)  
2107 - the latter is on the other hand a reasonable approximation, see below, *Weak focusing*  
2108 *approximation*. G. Floquet has established [19] that the two independent solutions  
2109 of Hill's second order differential equation have the form [16]

$$\left\{ \begin{array}{l} u_1(s) = \sqrt{\beta_u(s)} e^{i \int_0^s \frac{ds}{\beta_u(s)}} \\ du_1(s)/ds = \frac{i - \alpha_u(s)}{\beta_u(s)} u_1(s) \end{array} \right. \quad \text{and} \quad \left\{ \begin{array}{l} u_2(s) = u_1^*(s) \\ du_2(s)/ds = du_1^*(s)/ds \end{array} \right. \quad (9.12)$$

2110 wherein  $\beta_u(s)$  and  $\alpha_u(s) = -\beta'_u(s)/2$  are S-periodic functions, from what it results  
2111 that

$$u_{\frac{1}{2}}(s + S) = u_{\frac{1}{2}}(s) e^{\pm i \mu_u} \quad (9.13)$$

2112 wherein

$$\mu_u = \int_{s_0}^s \frac{ds}{\beta_u(s)} \quad (9.14)$$

2113 is the betatron phase advance at  $s$ , from the origin  $s_0$ . A real solution of Hill's  
2114 equation is the linear combination  $A u_1(s) + A^* u_2^*(s)$ . With  $A = \frac{1}{2} \sqrt{\varepsilon_u/\pi} e^{i\phi}$   
2115 following conventional notations,  $\phi$  the phase of the motion at the origin  $s = s_0$ , the  
2116 general solution of Eq. 9.11 writes

$$\left\{ \begin{array}{l} u(s) = \sqrt{\beta_u(s) \varepsilon_u/\pi} \cos\left(\int_{s_0}^s \frac{ds}{\beta_u} + \phi\right) \\ u'(s) = -\sqrt{\frac{\varepsilon_u/\pi}{\beta_u(s)}} \sin\left(\int_{s_0}^s \frac{ds}{\beta_u} + \phi\right) + \alpha_u(s) \cos\left(\int_{s_0}^s \frac{ds}{\beta_u} + \phi\right) \end{array} \right. \quad (9.15)$$

2117 An invariant of the motion, known as the Courant-Snyder invariant, is

$$\frac{1}{\beta_u(s)} \left[ u^2 + (\alpha_u(s)u + \beta_u(s)u')^2 \right] = \frac{\varepsilon_u}{\pi} \quad (9.16)$$

2118 At a given azimuth  $s$  of the periodic structure the observed turn-by-turn motion  
2119 lies on that ellipse (Fig. 9.10). The form and inclination of the ellipse depend on  
2120 the observation azimuth  $s$  via the respective local values of  $\alpha_u(s)$  and  $\beta_u(s)$ , but  
2121 its surface  $\varepsilon_u$  is invariant. Motion along the ellipse is clockwise, as can be figured  
2122 from Eq. 9.15 considering an observation azimuth  $s$  where the ellipse is upright,  
2123  $\alpha_u(s) = 0$ . The phase advance over a turn (from one position to the next on the  
2124 ellipse, Fig. 9.10) in an N-periodic ring yields the wave number

$$\nu_u = N \mu_u = \int_{s_0}^{s_0 + NS} \frac{ds}{\beta_u(s)} = N \int_{\text{period}} \frac{ds}{\beta_u(s)} \quad (9.17)$$

2125 *Weak focusing approximation*

2126 In a cylindrically symmetric structure a sinusoidal motion is the exact solution of the  
2127 first order differential equations of motion (Eqs. 4.15, 4.16, Classical Cyclotron Chap-  
2128 ter), the coefficients  $K_x = (1 - n)/R_0^2$  and  $K_y = n/R_0^2$  are constant (s-independent).  
2129 Adding drift spaces results in Hill's differential equation with periodic coefficient  
2130  $K(s + S) = K(s)$  (Eq. 9.11), and in a pseudo harmonic solution (Eq. 9.15). Due to the

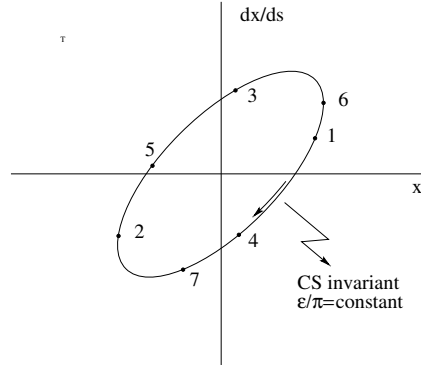


**Fig. 9.10** Courant-Snyder invariant and turn-by-turn harmonic motion along the invariant, observed at some azimuth  $s$ . The form and tilt-angle of the ellipse depend on the observation azimuth  $s$  but its surface  $\varepsilon_u$  is invariant

2131 weak focusing the beam envelope is only weakly modulated (see below), thus so is  
 2132  $\beta_u(s)$ . In a practical manner, the modulation of  $\beta_u(s)$  does not exceed a few percent,  
 2133 this justifies introducing the average value  $\overline{\beta_u}$  to approximate the phase advance by

$$\int_0^s \frac{ds}{\beta_u(s)} \approx \frac{s}{\overline{\beta_u}} = \nu_u \frac{s}{R} \quad (9.18)$$

2134 The right equality is obtained by applying this approximation to the phase advance  
 2135 per period, namely (Eq. 9.14)  $\mu_u = \int_{s_0}^{s_0+S} \frac{ds}{\beta_u(s)} \approx S/\overline{\beta_u}$ , and introducing the wave  
 2136 number of the N-period optical structure  $\nu_u = \frac{N\mu_u}{2\pi} = \frac{\text{phase advance over a turn}}{2\pi}$  so that

$$\overline{\beta_u} = \frac{R}{\nu_u} \quad (9.19)$$

2137 the wavelength of the betatron oscillation around the ring. With  $k \ll 1$  and using  
 2138 Eq. 9.23,

$$\overline{\beta_x} = \frac{\rho_0(1+k/2)}{\sqrt{1-n}}, \quad \overline{\beta_y} = \frac{\rho_0(1+k/2)}{\sqrt{n}} \quad (9.20)$$

2139 Substituting  $\nu_u \frac{s}{R}$  to  $\int \frac{ds}{\beta_u(s)}$  in Eq. 9.15 yields the approximate solution

$$\begin{cases} u(s) \approx \sqrt{\beta_u(s)\varepsilon_u/\pi} \cos\left(\nu_u \frac{s}{R} + \phi\right) \\ u'(s) \approx -\sqrt{\frac{\varepsilon_u/\pi}{\beta_u(s)}} \sin\left(\nu_u \frac{s}{R} + \phi\right) + \alpha_u(s) \cos\left(\nu_u \frac{s}{R} + \phi\right) \end{cases} \quad (9.21)$$

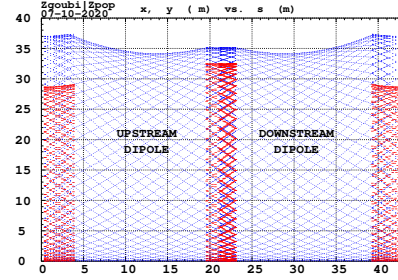
2140 *Beam envelopes*

2141 The beam envelope  $\hat{u}(s)$  (with  $u$  standing for  $x$  or  $y$ ) is determined by the particle of  
 2142 maximum invariant  $\varepsilon_u/\pi$ , it is given at all  $s$  by

$$\hat{u}_{\text{env}}(s) = \pm \sqrt{\beta_u(s) \frac{\mathcal{E}_u}{\pi}} \quad (9.22)$$

As  $\beta_u(s)$  is  $S$ -periodic, so is the envelope,  $\hat{u}(s+S) = \hat{u}(s)$ . In a cell with symmetries,

**Fig. 9.11** Multi-turn particle excursion along the ZGS 2-dipole 43 m cell. The motion extrema (Eq. 9.22) tangent the envelopes, respectively horizontal (red), and vertical (blue). Envelopes have the symmetry of the cell



2143 beam envelopes feature the same symmetries, as in Fig. 9.11 for instance: a symmetry  
 2144 with respect to the center of the cell; envelop extrema are at azimuth  $s$  of  $\beta_u(s)$   
 2145 extrema, *i.e.* where  $d\hat{u}(s)/ds \propto \beta'_u(s) = 0$  or  $\alpha_u = 0$  as  $\beta'_u = -2\alpha_u$ .  
 2146

#### 2147 Working point

2148 The “working point” of the synchrotron is the wave number couple  $(\nu_x, \nu_y)$  at which  
 2149 the accelerator is operated, it fully characterizes the focusing. In a structure with  
 2150 cylindrical symmetry (such as the Classical Cyclotron)  $\nu_x = \sqrt{1-n}$  and  $\nu_y = \sqrt{n}$   
 2151 (Eq. 4.17) so that  $\nu_x^2 + \nu_y^2 = 1$ : when the radial field index  $n$  is changed the working  
 2152 point stays on a circle of radius 1 in the stability diagram (or “tune diagram”,  
 2153 Fig. 9.12). If drift spaces are added, from Eqs. 9.19, 9.20, with  $1 + \frac{k}{2} \approx \sqrt{R/\rho_0}$   
 2154 (Eq. 9.6), it comes

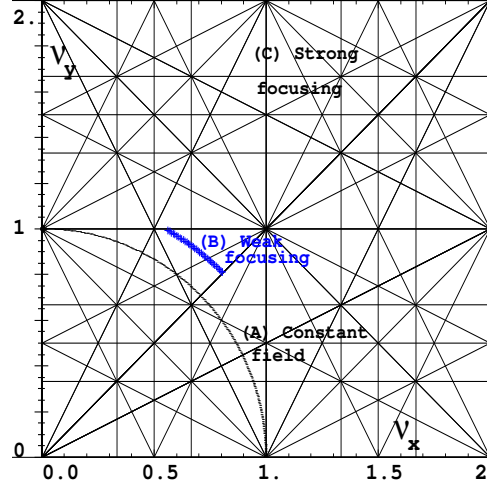
$$\nu_x \approx \sqrt{(1-n) \frac{R}{\rho_0}}, \quad \nu_y \approx \sqrt{n \frac{R}{\rho_0}}, \quad \nu_x^2 + \nu_y^2 \approx \frac{R}{\rho_0} \quad (9.23)$$

thus the working point is located on the circle of radius  $\sqrt{R/\rho_0} > 1$  (Fig. 9.12), tunes  
 can not exceed the limits

$$0 < \nu_{x,y} \lesssim \sqrt{R/\rho_0}$$

2155 Horizontal and vertical focusing are not independent (Eq. 9.11): if  $\nu_x$  increases then  
 2156  $\nu_y$  decreases and reciprocally. This is a lack of flexibility which the advent of strong  
 2157 focusing will overcome by providing two knobs allowing separate adjustment of the  
 2158 tunes.

**Fig. 9.12** Location of the working point in the tune diagram. (A) field with revolution symmetry:  $(\nu_x, \nu_y)$  is on a circle of radius 1; (B) sector field with field index  $0 < n < 1$  and drift spaces:  $(\nu_x, \nu_y)$  is on a circle of radius  $(\sqrt{R/\rho_0})$ ; (C) strong focusing, field index  $|n| \gg 1$ ,  $\nu_x$  and  $\nu_y$  are independent and large



#### 2159 Off-momentum orbits; periodic dispersion

2160 In the linear approximation in  $\Delta p/p_0$ , a momentum offset  $\Delta p = p - p_0$  changes  
 2161  $mv$  to  $mv(1 + \Delta p/p_0)$  in Eq. 9.8; this changes the horizontal equation of motion  
 2162 (Eq. 9.10) to

$$\frac{d^2x}{ds^2} + K_x x = \frac{1}{\rho_0} \frac{\Delta p}{p_0}, \quad \text{or} \quad \frac{d^2x}{ds^2} + K_x \left( x - \frac{1}{\rho_0 K_x} \frac{\Delta p}{p_0} \right) = 0 \quad (9.24)$$

2163 A change of variable  $x - \frac{1}{K_x \rho_0} \frac{\Delta p}{p_0} \rightarrow x$  (with  $1/\rho_0 K_x = \rho_0/(1-n)$ ) restores the  
 2164 unperturbed equation of motion; thus orbits of different momenta  $p = p_0 + \Delta p$  are  
 2165 distant

$$\Delta x = \frac{\rho_0}{1-n} \frac{\Delta p}{p_0} \quad (9.25)$$

2166 from the reference orbit (Fig. 9.8). Introduce the geometrical radius  $R = (1+k)\rho_0$   
 2167 (Eq. 9.6) to account for the added drifts; this yields the dispersion function

$$D_x = \frac{\Delta x}{\Delta p/p_0} \equiv \frac{\Delta R}{\Delta p/p_0} = \frac{R}{(1-n)(1+k)} = \frac{\rho_0}{1-n}, \quad \text{constant, positive} \quad (9.26)$$

2168  $D_x$  is the chromatic dispersion of the orbits, an  $s$ -independent quantity: in a structure  
 2169 with axial symmetry, comprising drift sections (Fig. 9.5) or not (classical and AVF  
 2170 cyclotrons for instance), the ratio  $\frac{\Delta x}{\rho_0 \Delta p/p_0}$  is independent of the azimuth  $s$ , the  
 2171 distance of a chromatic orbit to the reference orbit is constant around the ring.

2172 Given that  $n < 1$ ,

- 2173 - higher momentum orbits,  $p > p_0$ , have a greater radius,
- 2174 - lower momentum orbits,  $p < p_0$ , have a smaller radius.

2175 The horizontal motion of an off-momentum particle is a superposition of the  
 2176 betatron motion (solution of Hill's Eq. 9.21 with  $\delta p/p = 0$ ) and of a particular  
 2177 solution of the inhomogeneous equation ( $\delta p/p \neq 0$ ), namely

$$x(s) = \sqrt{\beta_u(s)\varepsilon_u/\pi} \cos\left(\nu_u \frac{s}{R} + \phi\right) + \frac{\rho_0}{1-n} \frac{\Delta p}{p_0} \quad (9.27)$$

2178 whereas the vertical motion is unchanged.

### 2179 *Chromatic orbit length*

2180 In an axially symmetric structure the difference in closed orbit length  $\Delta C = 2\pi\Delta R$   
 2181 resulting from the difference in momentum arises in the dipoles, as all orbits are  
 2182 parallel in the drifts (Fig. 9.5). Hence, from Eq. 9.26, the relative closed orbit  
 2183 lengthening factor, or momentum compaction

$$\alpha = \frac{\Delta C}{C} \Big/ \frac{\Delta p}{p_0} \equiv \frac{\Delta R}{R} \Big/ \frac{\Delta p}{p_0} = \frac{1}{(1-n)(1+k)} \approx \frac{1}{\nu_x^2} \quad (9.28)$$

2184 with  $k = Nl/\pi\rho_0$  (Eq. 9.6). Note that the relationship  $\alpha \approx 1/\nu_x^2$  between momentum  
 2185 compaction and horizontal wave number established for a revolution symmetry  
 2186 structure (Eq. 4.21) still holds when adding drifts.

## 2187 **9.1.2 Acceleration**

In a synchrotron, the field  $B$  is varied during acceleration (a function performed by the magnet power supply) concurrently with the variation of the bunch momentum  $p$  (a function performed by the accelerating cavity) in such a way that the beam is maintained on the design orbit. Given the energies involved, the magnet supply imposes its law  $B(t)$  (Fig. 9.13) and the cavity follows, the best it can. The accelerating voltage  $\hat{V}(t) = \sin \omega_{rf}t$  is maintained in synchronism with the revolution motion, its angular frequency satisfying

$$\omega_{rf} = h\omega_{rev} = h \frac{c}{R} \frac{B(t)}{\sqrt{\left(\frac{m_0}{q\rho}\right)^2 + B^2(t)}}$$

Typically, for a  $C = 2\pi R \approx 70$  m circumference ring (SATURNE I weak focusing synchrotron, Fig. 9.1; cf. Exercise 9.1, parameters in Tab. 9.1), from  $\beta = v/c \approx 0.09$  at injection (3.6 MeV protons) to  $\beta \approx 1$  at top energy (3 GeV), the revolution period  $T_{rev} = C/\beta c$  and frequency  $\omega_{rev}/2\pi = 1/T_{rev}$  span

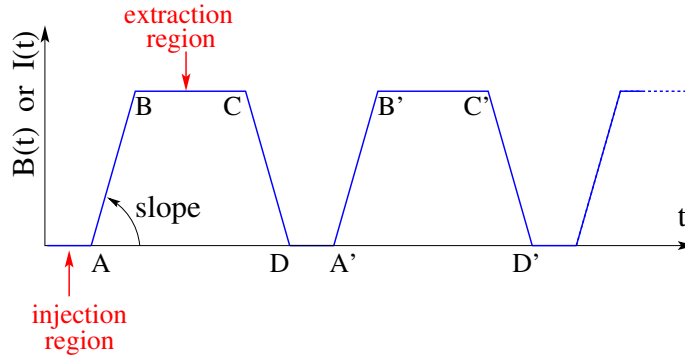


**Fig. 9.13** Cycling  $B(t)$  in a pulsed synchrotron. Ignoring saturation,  $B(t)$  is proportional to the magnet power supply current  $I(t)$ . Beam injection occurs at low field, in the region of A, extraction occurs at top energy, on the high field plateau. (AB): field ramp up (acceleration); (BC): flat top; (CD): field ramp down; (DA'): thermal relaxation. (AA'): repetition period;  $(1/AA')$ : repetition rate; *slope*: ramp velocity  $\dot{B} = dB/dt$  (Tesla/s).

$$\begin{cases} T_{\text{rev}} : 2.6 \mu\text{s} \rightarrow 23 \mu\text{s} \\ f_{\text{rev}} : 390 \text{ kHz} \rightarrow 4.3 \text{ MHz} \end{cases}$$

2188 *Energy gain*

2189 The variation of the particle energy over a turn amounts to the work of the force  
2190  $F = dp/dt = q\rho dB/dt$  on the charge at the cavity, namely

$$\Delta W = F \times 2\pi R = 2\pi R q \rho \dot{B} \quad (9.29)$$

In a slow-cycling synchrotron  $\dot{B}$  is usually constant over most of the acceleration cycle (Eq. 9.3), thus so is  $\Delta W$ . At SATURNE I for instance

$$\frac{\Delta W}{q} = 2\pi R \rho \dot{B} = 68.9 \times 8.42 \times 1.8 = 1044 \text{ volts}$$

The field ramp lasts

$$\Delta t = (B_{\text{max}} - B_{\text{min}})/\dot{B} \approx B_{\text{max}}/\dot{B} = 0.8 \text{ s}$$

The number of turns to the top energy ( $W_{\text{max}} \approx 3 \text{ GeV}$ ) is

$$N = \frac{W_{\text{max}}}{\Delta W} = \frac{3 \cdot 10^9 \text{ eV}}{1044 \text{ eV/turn}} \approx 3 \cdot 10^6 \text{ turns}$$

The dependence of particle mass on field writes



$$m(t) = \gamma(t)m_0 = \frac{q\rho}{c} \sqrt{\left(\frac{m_0}{qc\rho}\right)^2 + B(t)^2}$$

2191 *Adiabatic damping of the betatron oscillations*

Particle momentum increases at the accelerating gap, this results in a decrease of the amplitude of betatron oscillations (conversely, an increase if the cavity is decelerating). The mechanism is sketched in Fig. 9.14 (with  $u$  standing indifferently for the  $x$  or  $y$  coordinate): the slope, respectively before and after (index 2) the cavity is

$$\frac{du}{ds} = \frac{m \frac{du}{dt}}{m \frac{ds}{dt}} = \frac{p_u}{p_s}, \quad \left. \frac{du}{ds} \right|_2 = \left. \frac{m \frac{du}{dt}}{m \frac{ds}{dt}} \right|_2 = \frac{p_{u,2}}{p_{s,2}}$$

As the kick in momentum is longitudinal,  $dp_u/dt = 0$  thus  $p_{u,2} = p_u$ , the increase

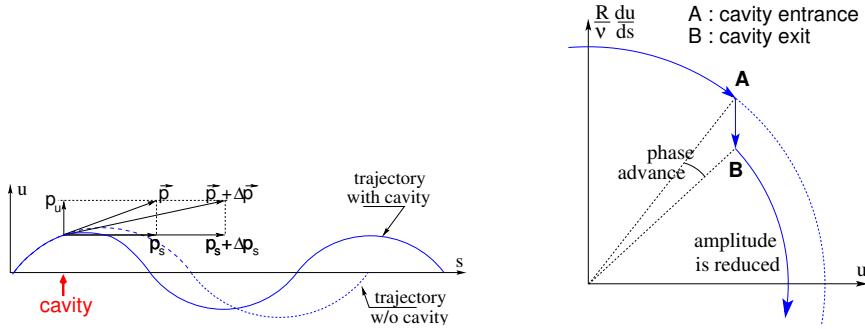


**Fig. 9.14** Adiabatic damping of betatron oscillations, here from trajectory incidence  $u' = p_u/p_s$  at cavity entrance, to  $u'_2 = p_u/(p_s + \Delta p_s)$  at cavity exit. In the transverse phase space: decrease of the particle phase space invariant resulting from  $\Delta \left( \frac{du}{ds} \right)$

in momentum is purely longitudinal,  $p_{s,2} = p_s + \Delta p$ . Thus

$$\left. \frac{du}{ds} \right|_2 = \frac{p_u}{p_s + \Delta p} \approx \frac{p_u}{p_s} \left( 1 - \frac{\Delta p}{p_s} \right)$$

and as a consequence the slope  $du/ds$  varies across the cavity,

$$\Delta \left( \frac{du}{ds} \right) = \left. \frac{du}{ds} \right|_2 - \frac{du}{ds} = - \frac{du}{ds} \frac{\Delta p_s}{p_s}$$

2192 The variation of the slope is proportional to the slope, with opposite sign if  $\Delta p/p > 0$   
 2193 (acceleration) thus a decrease of the slope. This variation has two consequences on  
 2194 the betatron oscillation (Fig. 9.14):

- 2195 - a change of the betatron phase,  
 2196 - a modification of the betatron amplitude.

2197 *Coordinate transport*

2198 at the cavity writes  $\begin{cases} u_2 = u \\ u'_2 \approx \frac{p_u}{p_s} (1 - \frac{dp}{p}) = u' (1 - \frac{dp}{p}) \end{cases}$ . In matrix form,  $\begin{pmatrix} u_2 \\ u'_2 \end{pmatrix} =$

2199  $[C] \begin{pmatrix} u \\ u' \end{pmatrix}$  with

$$[C] = \begin{bmatrix} 1 & 0 \\ 0 & 1 - \frac{dp}{p} \end{bmatrix} \quad (9.30)$$

2200 and  $\det[C] = 1 - \frac{dp}{p} \neq 1$ : the system is non-conservative, the surface of the beam  
 2201 ellipse in phase space is not conserved. Assume one cavity in the ring and note  
 2202  $[T] \times [C]$  the one-turn coordinate transport matrix with origin at entrance of the  
 2203 cavity. Its determinant is  $\det[T] \times \det[C] = \det[C] = 1 - \frac{dp}{p}$ ; the variation of  
 2204 the transverse ellipse surface satisfies  $\varepsilon_u = (1 - \frac{dp}{p_0})\varepsilon_0$  or, with  $d\varepsilon_u = \varepsilon_u - \varepsilon_0$ ,  
 2205  $\frac{d\varepsilon_u}{\varepsilon_u} = -\frac{dp}{p_0}$ , the solution of which is

$$p \varepsilon_u = \text{constant, or } \beta\gamma\varepsilon_u = \text{constant} \quad (9.31)$$

2206 Over  $N$  turns the coordinate transport matrix is  $[T_N] = ([T][C])^N$ , thus the ellipse  
 2207 surface changes by a factor  $\det[C]^N = (1 - \frac{dp}{p})^N \approx 1 - N\frac{dp}{p}$ .

2208 *Synchrotron motion; phase stability*

2209 “Synchrotron motion” designates the mechanism of phase stability, or longitudinal  
 2210 focusing (Fig. 9.15), that stabilizes the longitudinal motion of a particle in the vicinity  
 2211 of a synchronous phase,  $\phi_s$ , in virtue of

2212 (i) the presence of an accelerating cavity with its frequency indexed on the  
 2213 revolution time,

2214 (ii) with the bunch centroid positioned either on the rising slope of the oscillating  
 2215 voltage (low energy regime), or on the falling slope (high energy regime).

The synchronous (or “ideal”) particle follows the equilibrium trajectory around  
 the ring (the reference closed orbit, about which all other particles will undergo a  
 betatron oscillation), its velocity satisfies  $v(t) = \frac{qB\rho(t)}{m}$ ; at each turn it reaches the  
 accelerating gap when the oscillating voltage is at the synchronous phase  $\phi_s$ , and  
 undergoes an energy gain

$$\Delta W = q\hat{V} \sin \phi_s$$

The condition  $|\sin \phi_s| < 1$  imposes a lower limit to the cavity voltage for acceleration  
 to happen, namely, after Eq. 9.29,

$$\hat{V} > 2\pi R\rho\dot{B}$$

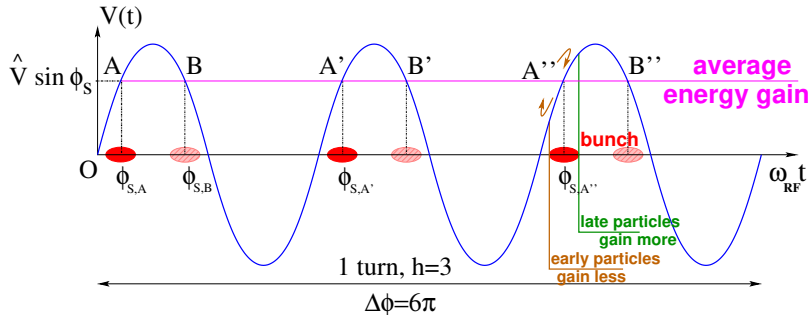


**Fig. 9.15** A sketch of the mechanism of phase stability,  $h = 3$  in this example. Below transition phase stability occurs for a synchronous phase taken at either one of A, A', A'' arrival times at the gap: a particle with a little greater energy compared to the synchronous particle goes around the ring more rapidly than the latter: if both are launched together, the former arrives earlier at the voltage gap (at  $\phi < \phi_{s,A}$ ) and thus experiences weaker acceleration; a particle with a little lower energy compared to the synchronous particle, is slower, it arrives at the gap later,  $\phi > \phi_{s,A}$ , and thus experiences greater voltage; in both cases the particle is pulled towards the synchronous phase, this results in an overall stable oscillatory motion around the synchronous phase. Beyond transition the stable phase is at either one of B, B', B'' locations: a particle which is less energetic than the synchronous particle arrives earlier,  $\phi < \phi_{s,B}$ , so experiencing a greater voltage, and inversely, resulting in overall stable synchrotron motion.

Referring to Fig. 9.15, the synchronous phase can be placed on the left (A A' A''... series in the Figure, or on the right (B B' B''... series) of the oscillating voltage crest. One and only one of these two possibilities, and which one depending upon the optical lattice and on particle energy, ensures that particles in a bunch remain grouped in the vicinity of the synchronous particle. The transition is between two time-of-flight regimes: a particle which gains momentum compared to the synchronous particle has a greater velocity, while

- in the high bunch energy regime the increase in path length around the ring is faster than the increase in velocity (velocity essentially does not even change in ultrarelativistic regime), a revolution around the ring takes more time (this is the classical cyclotron and synchrocyclotron regime, and as well the high energy electron synchrotron regime); consider such a particle, arriving at the accelerating gap late ( $\phi(t) > \phi_s$ ), in order for it to be pulled toward bunch center (*i.e.*, take less time around the ring) it has to undergo deceleration; this is the B series, above transition;
- in the low bunch energy regime velocity increase is faster than path length increase, thus a revolution around the ring is faster; consider such a particle, arriving at the accelerating gap early ( $\phi(t) < \phi_s$ ), in order for it to be pulled toward bunch center (*i.e.*, take more time around the ring) it has to be slowed down, it has to undergo deceleration; this is the A series, below transition.

2235 *Transition energy*

2236 The transition between the two time-of-flight regimes occurs at  $\frac{dT_{\text{rev}}}{T_{\text{rev}}} = 0$ . With  
 2237  $T = 2\pi/\omega = C/v$ , this can be written  $\frac{d\omega_{\text{rev}}}{\omega_{\text{rev}}} = -\frac{dT_{\text{rev}}}{T_{\text{rev}}} = \frac{dv}{v} - \frac{dC}{C}$ . With  $\frac{dv}{v} = \frac{1}{\gamma^2} \frac{dp}{p}$   
 2238 and momentum compaction  $\alpha = \frac{dC}{C} / \frac{dp}{p}$ , (Eq. 9.28), this can be written

$$\frac{d\omega_{\text{rev}}}{\omega_{\text{rev}}} = -\frac{dT_{\text{rev}}}{T_{\text{rev}}} = \left( \frac{1}{\gamma^2} - \alpha \right) \frac{dp}{p} = \eta \frac{dp}{p} \quad (9.32)$$

2239 which introduces the phase-slip factor

$$\eta = \overbrace{\frac{1}{\gamma^2}}^{\text{kinematics}} - \underbrace{\alpha}_{\text{lattice}} = \frac{1}{\gamma^2} - \frac{1}{\gamma_{\text{tr}}^2} \quad (9.33)$$

2240 The transition  $\gamma_{\text{tr}}$  appears to be a property of the lattice.

2241 In a weak focusing lattice  $\gamma_{\text{tr}} = 1/\sqrt{\alpha} \approx v_x$  (Eqs. 4.21, 9.28), thus the phase  
 2242 stability regime is

$$\begin{aligned} &\text{below transition, i.e. } \phi_s < \pi/2, \quad \text{if } \gamma < v_x \\ &\text{above transition, i.e. } \phi_s > \pi/2, \quad \text{if } \gamma > v_x \end{aligned} \quad (9.34)$$

2243 In a weak focusing synchrotron the horizontal tune  $\nu_x = \sqrt{(1-n)R/\rho_0}$  (Eq. 9.23)  
 2244 may be  $\geq 1$ , and subsequently  $\gamma_{\text{tr}} > 1$  is a possibility. There is no transition-gamma if  
 2245  $\nu_x < 1$ . At SATURNE I for instance, with  $\nu_x \approx 0.7$  (Tab. 9.1) thus  $\gamma_{\text{tr}} < 1$ , ramping  
 2246 in energy did not require transition-gamma crossing<sup>3</sup>.

### 2247 9.1.3 Depolarizing Resonances

2248 The field index is essentially zero in the ZGS, transverse focusing is ensured by  
 2249 wedge angles at the ends of the height dipoles, the only location where non-zero  
 2250 radial field components are found. The latter are weak, as a consequence so are  
 2251 depolarizing resonances: “As we can see from the table, the transition probability  
 2252 [from spin state  $\psi_{1/2}$  to spin state  $\psi_{-1/2}$ ] is reasonably small up to  $\gamma = 7.1$ ” [12], i.e.  
 2253  $G\gamma = 12.73$ ,  $p = 6.6$  GeV/c; the table referred to stipulates a transition probability  
 2254  $P_{\frac{1}{2}, -\frac{1}{2}} < 0.042$ , whereas resonances beyond that energy range feature  $P_{\frac{1}{2}, -\frac{1}{2}} > 0.36$ .

<sup>3</sup> Transition-gamma crossing, or “gamma jump”, is a common beam manipulation during acceleration in strong focusing synchrotrons, it requires an RF phase jump, the technique is addressed in Chapter 10.

2255 Beam depolarization up to 6 GeV/c, under the effect of these resonances, is illustrated  
 2256 in Fig. 9.16.

2257 In a synchrotron using gradient dipoles, particles experience radial fields  $B_x(y) =$   
 2258  $-n \frac{B_0}{\rho_0} y$  as they undergo vertical betatron oscillations [12, 20, 21]. As  $n$  is small these  
 2259 radial field components are weak, and so is their effect on spin motion.

Assuming a defect-free ring, the vertical betatron motion excites “intrinsic” spin resonances, located at

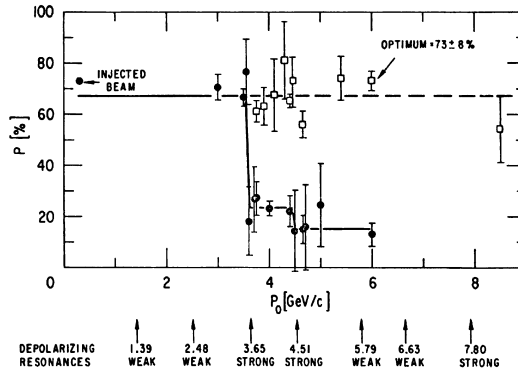
$$G\gamma_R = k P \pm \nu_y$$

with  $k$  an integer and  $P$  the period of the ring. In the ZGS for instance,  $\nu_y \approx 0.8$  (Tab. 9.2), the ring is  $P=4$ -periodic, thus  $G\gamma_R = 4k \pm 0.8$ . Strongest resonances are located at

$$G\gamma_R = mk P \pm \nu_y$$

2260 with  $m$  the number of cells per superperiod [22, Sec. 3.II]. In the ZGS,  $m=2$  thus  
 2261 strongest resonances occur at  $G\gamma_R = 2 \times 4k \pm 0.8 = 7.2$  ( $p = 3.65$  GeV/c), 8.8 (4.51 GeV/c), 15.2 (7.9 GeV/c), ... (Fig. 9.16).

**Fig. 9.16** Depolarizing intrinsic resonance landscape up to 9 GeV/c at the ZGS (solid circles) [23]. Systematic resonances are located at  $G\gamma_R = 4 \times \text{integer} \pm \nu_y$ , stronger ones at  $G\gamma_R = 8 \times \text{integer} \pm \nu_y$ . A tune jump was applied to preserve polarization when crossing strong resonances (empty circles)



2262 In the presence of vertical orbit defects, non-zero periodic transverse fields are experienced along the closed orbit, they excite “imperfection” depolarizing resonances, located at

$$G\gamma_R = k$$

with  $k$  an integer. In the case of systematic defects the periodicity of the orbit is that of the lattice,  $P$ , imperfection resonances are located at  $G\gamma_R = kP$ . Strongest imperfection resonances are located at [22, Sec. 3.II]

$$G\gamma_R = mk P$$

2263 Crossing a depolarizing resonance of strength  $\epsilon_R$  causes a loss of polarization  
 2264 given by (Froissart-Stora formula [24])

$$\frac{P_f}{P_i} = 2e^{-\frac{\pi}{2} \frac{|\epsilon_R|^2}{\alpha}} - 1 \quad (9.35)$$

2265 from a value  $P_i$  upstream to an asymptotic value  $P_f$  downstream of the resonance.  
 2266 This assumes an isolated resonance, crossed at an energy gain  $\Delta E$  per turn, with a  
 2267 crossing speed

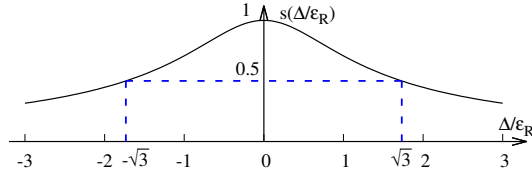
$$\alpha = G \frac{d\gamma}{d\theta} = \frac{1}{2\pi} \frac{\Delta E}{M} \quad (9.36)$$

2268 *Spin precession axis. Resonance width*

2269 Consider the spin vector  $\mathbf{S}(\theta) = (S_\eta, S_\xi, S_y)$  of a particle in the laboratory frame,  
 2270 with  $\theta$  the orbital angle around the accelerator. Introduce the projection  $s(\theta)$  of  $\mathbf{S}$  in  
 2271 the median plane

$$s(\theta) = S_\eta(\theta) + jS_\xi(\theta) \quad (\text{and } S_y^2 = 1 - s^2) \quad (9.37)$$

2272 **Fig. 9.17** Modulus of the  
 2273 horizontal spin component.  
 2274  $s = 1/2$  at distance  $\Delta =$   
 $\pm\sqrt{3}\epsilon_R$  from  $G\gamma_R$



2272

2273 It can be shown that in the case of a stationary solution of the spin motion, viz.  
 2274 the spin precession axis,  $s$  satisfies [21] (Fig. 9.17)

$$s^2 = \frac{1}{1 + \frac{\Delta^2}{|\epsilon_R|^2}} \quad (9.38)$$

2275 with  $\Delta = G\gamma - G\gamma_R$  the distance to the resonance. The resonance width is a measure  
 2276 of its strength (Fig. 9.18). The quantity of interest is the angle,  $\phi$ , of the spin  
 2277 precession direction to the vertical axis, given by (Fig. 9.18)

$$\cos \phi(\Delta) \equiv S_y(\Delta) = \sqrt{1 - s^2} = \frac{\Delta/|\epsilon_R|}{\sqrt{1 + \Delta^2/|\epsilon_R|^2}} \quad (9.39)$$

2278 On the resonance,  $\Delta = 0$ , the spin precession axis lies in the bend plane:  $\phi = \pm\pi/2$ .  
 2279  $S_y = 0.99$  (1% depolarization) corresponds to a distance to the resonance  $\Delta = 7|\epsilon_R|$ ,  
 2280 spin precession axis at an angle  $\phi = \arccos(0.99) = 8^\circ$  from the vertical.

2281 Conversely, given  $S_y$ ,

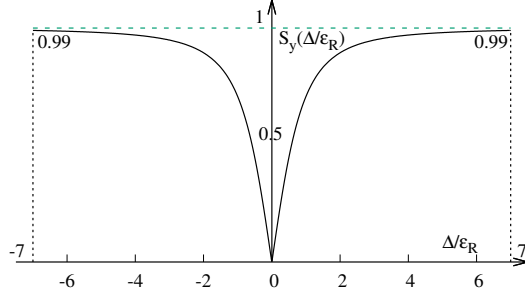


**Fig. 9.18** Dependence of polarization on the distance to the resonance. For instance  $S_y = 0.99$ , 1% depolarization, corresponds to  $\Delta = 7|\epsilon_R|$ . On the resonance,  $\Delta = 0$ , the precession axis lies in the median plane,  $S_y = 0$

$$\frac{\Delta^2}{|\epsilon_R|^2} = \frac{S_y^2}{1 - S_y^2} \tag{9.40}$$

The precession axis is common to all spins,  $S_y$  is a measure of the polarization along the vertical axis,

$$S_y = \frac{N^+ - N^-}{N^+ + N^-}$$

2282 wherein  $N^+$  and  $N^-$  denote the number of particles in spin states  $\frac{1}{2}$  and  $-\frac{1}{2}$  respectively.  
2283

2284 *Spin motion through weak resonances*

Depolarizing resonances are weak up to several GeV in a weak focusing synchrotron, as the radial and/or longitudinal fields, which stem from a small radial field index and from dipole fringe fields, are weak. Spin motion  $S_y(\theta)$  through a resonance in that case can be assumed to satisfy  $S_{y,f} \approx S_{y,i}$ , with  $S_{y,f}$  and  $S_{y,i}$  the asymptotic vertical spin component values respectively upstream and downstream of the resonance). As a consequence it can be calculated in terms of the Fresnel integrals [20, 21]

$$C(x) = \int_0^x \cos\left(\frac{\pi}{2}t^2\right) dt, \quad S(x) = \int_0^x \sin\left(\frac{\pi}{2}t^2\right) dt$$

2285 namely, with the origin of the orbital angle is taken at the resonance (Fig. 9.19),

$$\begin{aligned} \text{if } \theta < 0 : \left(\frac{S_y(\theta)}{S_{y,i}}\right)^2 &= 1 - \frac{\pi}{\alpha} |\epsilon_R|^2 \left\{ \left[0.5 - C\left(-\theta\sqrt{\frac{\alpha}{\pi}}\right)\right]^2 + \left[0.5 - S\left(-\theta\sqrt{\frac{\alpha}{\pi}}\right)\right]^2 \right\} \\ \text{if } \theta > 0 : \left(\frac{S_y(\theta)}{S_{y,i}}\right)^2 &= 1 - \frac{\pi}{\alpha} |\epsilon_R|^2 \left\{ \left[0.5 + C\left(\theta\sqrt{\frac{\alpha}{\pi}}\right)\right]^2 + \left[0.5 + S\left(\theta\sqrt{\frac{\alpha}{\pi}}\right)\right]^2 \right\} \end{aligned} \tag{9.41}$$

2286 In the asymptotic limit,

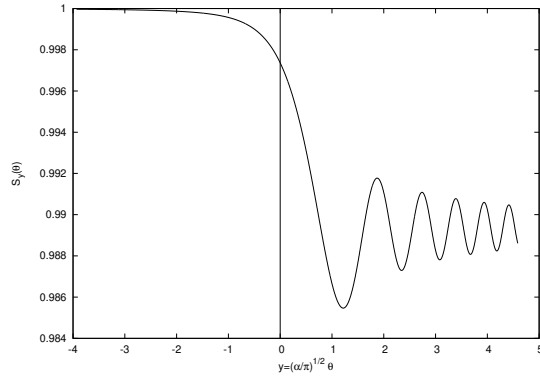


**Fig. 9.19** Vertical component of spin motion  $S_y(\theta)$  through a weak depolarizing resonance (after Eq. 9.41). The vertical bar is at the location of the resonance, which coincides with the origin of the orbital angle

$$\frac{S_y(\theta)}{S_{y,i}} \xrightarrow{\theta \rightarrow \infty} 1 - \frac{\pi}{\alpha} |\epsilon_R|^2 \tag{9.42}$$

2287 which identifies with the development of Froissart-Stora formula  $P_f/P_i =$   
 2288  $2 \exp(-\frac{\pi}{2} \frac{|\epsilon_R|^2}{\alpha}) - 1$  to the first order in  $|\epsilon_R|^2/\alpha$ . This approximation holds in the  
 2289 limit that higher order terms can be neglected:  $|\epsilon_R|^2/\alpha \ll 1$ .

## 2290 9.2 Exercises

### 2291 9.1 Construct SATURNE I (weak index) synchrotron. Spin Resonances

2292 Solution: page 304

2293 In this exercise, SATURNE I weak focusing 3 GeV synchrotron is modeled. Spin  
 2294 resonances in a weak dipole gradient lattice are studied.

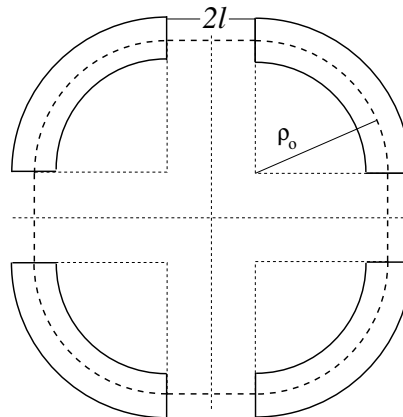


**Fig. 9.20** A schematic layout of SATURNE I, a  $2\pi/4$  axial symmetry structure, comprised of 4 radial field index 90 deg dipoles and 4 drift spaces. The cell in the simulation exercises is taken as a  $\pi/4$  quadrant: l-drift/90°-dipole/l-drift



**Table 9.1** Parameters of SATURNE I weak focusing synchrotron [25].  $\rho_0$  denotes the reference bending radius in the dipole; the reference orbit, field index, wave numbers, etc., are taken along that radius

Orbit length, $C$	cm	6890
Average radius, $R = C/2\pi$	cm	1096.58
Straight section length, $2l$	cm	400
Magnetic radius, $\rho_0$	cm	841.93
$R/\rho_0$		1.30246
Field index $n$ , nominal value		0.6
Wave numbers, $\nu_x; \nu_y$		0.724; 0.889 **** verif wrt. simul
Stability limit		$0.5 < n < 0.757$
Injection energy	MeV	3.6
Field at injection	kG	0.326
Top energy	GeV	2.94
$\dot{B}$	kG/s	18
Field at top energy, $B_{\max}$	kG	14.9
$B_{\max}\rho$	T m	13
Field ramp at injection	kG/s	20
Synchronous energy gain	keV/turn	1.160
RF harmonic		2

2295 (a) Construct a model of SATURNE I  $90^\circ$  cell dipole in the hard-edge model,  
 2296 using DIPOLE. Use the parameters given in Tab. 9.1, and Fig. 10.7 as a guidance. In  
 2297 order to allow beam monitoring, split the dipole in two  $45^\circ$  deg halves. It is judicious  
 2298 to take  $RM=841.93$  cm in DIPOLE, as this is the reference radius for the definition  
 2299 of the radial index. Take an integration step size in centimeter range - small enough  
 2300 to ensure numerical convergence, as large as doable for fast multiturn raytracing.

2301 Validate the model by producing the  $6 \times 6$  transport matrix of the cell dipole  
 2302 (MATRIX[IFOC=0] can be used for that, with OBJET[KOBJ=5] to define a proper  
 2303 set of paraxial initial coordinates) and checking against theory (Sect. 15.2, Eq. 15.6).

2304 (b) Construct a model of SATURNE I cell, with origin at the center of the drift.  
 2305 Find the closed orbit, that particular trajectory which has all its coordinates zero in  
 2306 the drifts: use DIPOLE[KPOS] to cancel the closed orbit coordinates at DIPOLE  
 2307 ends. While there, check the expected value of the dispersion (Eq. 9.26) and of  
 2308 the momentum compaction (Eq. 9.28), from the raytracing of a chromatic closed  
 2309 orbit - *i.e.*, the orbit of an off-momentum particle. Plot these two orbits (on- and  
 2310 off-momentum), over a complete turn around the ring, on a common graph.

2311 Compute the cell periodic optical functions and tunes, using either MA-  
 2312 TRIX[IFOC=11] or TWISS; check their values against theory. Check consistency  
 2313 with previous dispersion function and momentum compaction outcomes.

2314 Move the origin of the lattice at a different azimuth  $s$  along the cell: verify that,  
 2315 while the transport matrix depends on the origin, its trace does not.

2316 Produce a graph of the optical functions (betatron functions and dispersion) along  
 2317 the cell. Check the expected average values of the betatron functions (Eq. 9.20).

2318 Produce a scan of the tunes over the field index range  $0.5 \leq n \leq 0.757$ . RE-  
 2319 BELOTE can be used to repeatedly change  $n$  over that range. Superimpose the  
 2320 theoretical curves  $\nu_x(n)$ ,  $\nu_y(n)$ .

(c) Justify considering the betatron oscillation as sinusoidal, namely,

$$y(\theta) = A \cos(\nu_y \theta + \phi)$$

2321 wherein  $\theta = s/R$ ,  $R = \oint ds/2\pi$ .

2322 (d) Launch a few particles evenly distributed on a common paraxial horizontal  
2323 Courant-Snyder invariant, vertical motion taken null (OBJET[KOBJ=8] can be used),  
2324 for a single pass through the cell. Store particle data along the cell in zgoubi.plt,  
2325 using DIPOLE[IL=2] and DRIFT[split,N=20,IL=2]. Use these to generate a graph  
2326 of the beam envelopes.

2327 Using Eq. 9.22 compare with the results obtained in (b). Find the minimum  
2328 and maximum values of the betatron functions, and their azimuth  $s(\min[\beta_x])$ ,  
2329  $s(\max[\beta_x])$ . Check the latter against theory.

2330 Repeat for the vertical motion, taking  $\varepsilon_x = 0$ ,  $\varepsilon_y$  paraxial.

2331 Repeat, using, instead of several particles on a common invariant, a single particle  
2332 traced over a few tens of turns.

2333 (e) Produce an acceleration cycle from 3.6 MeV to 3 GeV, for a few particles  
2334 launched on a common  $10^{-4} \pi m$  initial invariant in each plane. Ignore synchrotron  
2335 motion (CAVITE[IOPT=3] can be used in that case). Take a peak voltage  $\hat{V} = 200$  kV  
2336 (unrealistic though, as it would result in a nonphysical  $\hat{B}$  (Eq. 9.29)) and synchronous  
2337 phase  $\phi_s = 150$  deg (justify  $\phi_s > \pi/2$ ).

2338 Check the betatron damping over the acceleration range: compare with theory  
2339 (Eq. 9.31).

2340 How close to symplectic the numerical integration is (it is by definition *not*  
2341 symplectic, being a truncated Taylor series method [26, Eq. 1.2.4]), depends on the  
2342 integration step size, and on the size of the flying mesh in the DIPOLE method [26,  
2343 Fig. 20]; check a possible departure of the betatron damping from theory as a function  
2344 of these parameters.

2345 Produce a graph of the horizontal and vertical wave number values over the  
2346 acceleration cycle.

2347 (f) Some spin motion, now. Adding SPNTRK at the beginning of the sequence  
2348 will ensure spin tracking.

2349 Based on the file worked out for question (d), simulate the acceleration of a single  
2350 particle, through the intrinsic resonance  $G\gamma_R = 4 - \nu_Z$ , from a few thousand turns  
2351 upstream to a few thousand turns downstream. On a common graph, plot  $S_y(\text{turn})$   
2352 for a few different values of the vertical betatron invariant (the horizontal invariant  
2353 value does not matter - explain that statement, it can be taken zero).

2354 (g) Produce a graph of the average value of  $S_Z$  over a 200 particle set, as a function  
2355 of  $G\gamma$ , across the  $G\gamma_R = 4 - \nu_Z$  resonance. Indicate on that graph the location of  
2356 the resonant  $G\gamma_R$  values.

2357 Perform this resonance crossing for five different values of the particle invariant:  
2358  $\varepsilon_Z/\pi = 2, 10, 20, 40, 200 \mu m$ . Compute  $P_f/P_i$  in each case, check the dependence  
2359 on  $\varepsilon_Z$  against theory.

2360 Compute the resonance strength,  $\varepsilon_Z$ , from these trackings.

2361 Re-do this crossing simulation for a different crossing speed (take for instance  
2362  $\hat{V} = 10\text{kV}$ ) and a couple of vertical invariant values, compute  $P_f/P_i$  so obtained.  
2363 Check the crossing speed dependence of  $P_f/P_i$  against theory.

2364 (h) Show that the previous weak resonance crossings ( $P_f/P_i \approx 1$ ) satisfies  
2365 Eq. 9.41. Match the tracking data to the latter to get the vertical betatron tune  $\nu_y$ , the  
2366 location of the resonance  $G\gamma_R$ , and its strength.

2367 (i) Track a few particles at fixed energy, at distances from the resonance  $G\gamma_R =$   
2368  $4 - \nu_y$  of up to a  $7 \times \epsilon_R$  (this distance corresponds to 1% depolarization).

2369 Produce on a common graph the spin motion  $S_Z(\text{turn})$  for all these particles, as  
2370 observed at some azimuth along the ring.

2371 Produce a graph of  $\langle S_y \rangle|_{\text{turn}}(\Delta)$  (as in Fig. 9.18).

Produce the vertical betatron tune  $\nu_y$ , the location of the resonance  $G\gamma_R$ , and its  
strength, obtained from a match of these tracking trials to (Eq. 9.39)

$$\langle S_y \rangle (\Delta) = \frac{\Delta}{\sqrt{|\epsilon_R|^2 + \Delta^2}}$$

## 2372 9.2 Construct the ZGS (zero-gradient) synchrotron. Spin Resonances

2373 Solution: page 328

2374 In this exercise, the ZGS 12 GeV synchrotron is modeled. Spin resonances in a  
2375 zero-gradient, wedge focusing synchrotron are studied.

2376 A photo taken in the ZGS tunnel is given in Fig. 9.4; a schematic layout of the ring  
2377 is shown in Fig. 9.21, and a sketch of the double dipole cell in Fig. 9.22. Table 9.2  
2378 details the parameters of the synchrotron resorted to in these simulations.

2379 (a) Construct a model of ZGS  $45^\circ$  cell dipole in the hard-edge model, using  
2380 DIPOLE. Use the parameters given in Tab. 9.2, and Figs. 9.21, 9.22 as a guidance.  
2381 In order to allow beam monitoring, split the dipole in two  $22.5^\circ$  deg halves. Take the  
2382 closed orbit radius as the reference  $RM=2076$  cm in DIPOLE: it will be assumed  
2383 that the orbit is the same at all energies<sup>4</sup>. Take an integration step size in centimeter  
2384 range - small enough to ensure numerical convergence, as large as doable for fast  
2385 multiturn raytracing.

2386 Validate the model by producing the  $6 \times 6$  transport matrices of both dipole  
2387 (MATRIX[IFOC=0] can be used for that, with OBJET[KOBJ=5] to define a proper  
2388 set of paraxial initial coordinates) and checking against theory (Sect. 15.2, Eq. 15.6).

2389 Add fringe fields in DIPOLE[ $\lambda, C_0 - C_5$ ], the rest if the exercise will use that  
2390 model. Take fringe field extent and coefficient values

$$\lambda = 60 \text{ cm } C_0 = 0.1455, C_1 = 2.2670, C_2 = -0.6395, C_3 = 1.1558, C_4 = C_5 = 0 \quad (9.43)$$

2391 ( $C_0 - C_5$  determine the shape of the field fall-off, they have been computed from a  
2392 typical measured field profile  $B(s)$ ).

<sup>4</sup> Note that in reality the reference orbit in ZGS moved outward during acceleration [27].

2393 (b) Construct a model of ZGS cell accounting for dipole fringe fields, with origin  
 2394 at the center of the long drift. In doing so, use DIPOLE[KPOS] to cancel the closed  
 2395 orbit coordinates at DIPOLE ends.

2396 Compute the periodic optical functions at cell ends, and cell tunes, using MA-  
 2397 TRIX[IFOC=11]; check their values against theory.

2398 Move the origin at the location (azimuth  $s$  along the cell) of the betatron functions  
 2399 extrema: verify that, while the transport matrix depends on the origin, its trace does  
 2400 not. Verify that the local betatron function extrema, and the dispersion function, have  
 2401 the expected values.

2402 Produce a graph of the optical functions (betatron functions and dispersion) along  
 2403 the cell.

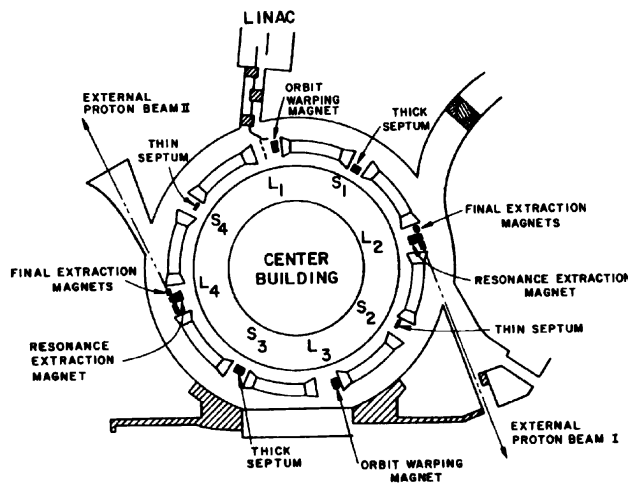


Fig. 9.21 A schematic layout of the ZGS [23], a  $\pi/2$ -periodic structure, comprised of 8 zero-index dipoles, 4 long and 4 short straight sections

2404 (c) Additional verifications regarding the model.

2405 Produce a graph of the field  $B(s)$

2406 - along the on-momentum closed orbit, and along off-momentum chromatic closed  
 2407 orbits, across a cell;

2408 - along orbits at large horizontal excursion;

2409 - along orbits at large vertical excursion.

2410 For all these cases, verify qualitatively, from the graphs, that  $B(s)$  appears as  
 2411 expected.

(d) Justify considering the betatron oscillation as sinusoidal, namely,

$$y(\theta) = A \cos(\nu_y \theta + \phi)$$

2412 wherein  $\theta = s/R$ ,  $R = \oint ds/2\pi$ .

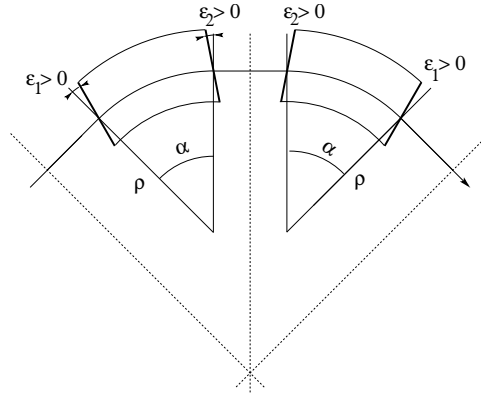


**Fig. 9.22** A sketch of ZGS cell layout. In defining the entrance and exit faces (EFBs) of the magnet, beam goes from left to right. Wedge angles at the long straight sections ( $\varepsilon_1$ ) and at the short straight sections ( $\varepsilon_2$ ) are different

**Table 9.2** Parameters of the ZGS weak focusing synchrotron after Refs. [27, 28] [23, pp.288-294,p. 716] (2nd column, when they are known) and in the present simplified model and numerical simulations (3rd column). Note that the actual orbit moves during ZGS acceleration cycle, tunes change as well - this is not taken into account in the present modeling, for simplicity

		<b>From Refs. [27, 28]</b>	<b>Simplified model</b>
Injection energy	MeV		50
Top energy	GeV		12.5
$G\gamma$ span			1.888387 - 25.67781
Length of central orbit	m	171.8	170.90457
Length of straight sections, total	m	41.45	40.44
<i>Lattice</i>			
Wave numbers $\nu_x; \nu_y$		0.82; 0.79	0.849; 0.771
Max. $\beta_x; \beta_y$	m		32.5; 37.1
<i>Magnet</i>			
Length	m	16.3	16.30486 (magnetic)
Magnetic radius	m	21.716	20.76
Field min.; max.	kG	0.482; 21.5	0.4986; 21.54
Field index			0
Yoke angular extent	deg	43.02590	45
Wedge angle	deg	$\approx 10$	13 and 8
<i>RF</i>			
Rev. frequency	MHz	0.55 - 1.75	0.551 - 1.751
RF harmonic $h = \omega_{rf} / \omega_{rev}$			8
Peak voltage	kV	20	200
B-dot, nominal/max.	T/s	2.15/2.6	
Energy gain, nominal/max.	keV/turn	8.3/10	100
Synchronous phase, nominal	deg		150
<i>Beam</i>			
$\varepsilon_x; \varepsilon_y$ (at injection)	$\pi \mu\text{m}$		25; 150
Momentum spread, rms			$3 \times 10^{-4}$
Polarization at injection	%	$> 75$	100
Radial width of beam (90%), at inj.	inch	2.5	$\sqrt{\beta_x \varepsilon_x / \pi} = 1.1$

2413 (e) Produce an acceleration cycle from 50 MeV to 17 GeV about, for a few particles  
2414 launched on a common  $10^{-5} \pi\text{m}$  vertical initial invariant, with small horizontal  
2415 invariant. Ignore synchrotron motion (CAVITE[IOPT=3] can be used in that case).  
2416 Take a peak voltage  $\hat{V} = 200\text{ kV}$  (this is unrealistic but yields 10 times faster  
2417 computing than the actual  $\hat{V} = 20\text{ kV}$ , Tab. 9.2) and synchronous phase  $\phi_s = 150\text{ deg}$   
2418 (justify  $\phi_s > \pi/2$ ). Add spin, using SPNTRK, in view of the next question, (f).

2419 Check the accuracy of the betatron damping over the acceleration range, compared  
2420 to theory. How close to symplectic the numerical integration is (it is by definition  
2421 *not* symplectic), depends on the integration step size, and on the size of the flying  
2422 mesh in the DIPOLE method [26, Fig. 20]; check a possible departure of the betatron  
2423 damping from theory as a function of these parameters.

2424 Produce a graph of the evolution of the horizontal and vertical wave numbers  
2425 during the acceleration cycle.

2426 (f) Using the raytracing material developed in (e): produce a graph of the vertical  
2427 spin component of the particles, and the average value over that 200 particle set, as  
2428 a function of  $G\gamma$ . Indicate on that graph the location of the resonant  $G\gamma_R$  values.

- 2429 (g) Based on the simulation file used in (f), simulate the acceleration of a single  
 2430 particle, through one particular intrinsic resonance, from a few thousand turns  
 2431 upstream to a few thousand turns downstream.
- 2432 Perform this resonance crossing for different values of the particle invariant.  
 2433 Determine the dependence of final/initial vertical spin component value, on the  
 2434 invariant value; check against theory.
- 2435 Re-do this crossing simulation for a different crossing speed. Check the crossing  
 2436 speed dependence of final/initial vertical spin component so obtained, against theory.
- 2437 (h) Introduce a vertical orbit defect in the ZGS ring.  
 2438 Find the closed orbit.
- 2439 Accelerate a particle launched on that closed orbit, from 50 MeV to 17 GeV about,  
 2440 produce a graph of the vertical spin component.
- 2441 Select one particular resonance, reproduce the two methods of (g) to check the  
 2442 location of the resonance at  $G\gamma_R = \text{integer}$ , and to find its strength.

## 2443 References

- 2444 1. Veksler, V.: A new method of acceleration of relativistic particles. J. of Phys. USSR 9 153-158  
 2445 (1945)
- 2446 2. McMillan, E. M.: The Synchrotron. Phys. Rev. 68 143-144 (1945)
- 2447 3. Goward, F. K., and Barnes, D. E.: Experimental 8 MeV synchrotron for electron acceleration.  
 2448 Nature 158, 413 (1946)
- 2449 4. Richardson, J.R., et al.: Frequency Modulated Cyclotron. Phys. Rev. 69: 669 (1946)
- 2450 5. Kerst, D. W.: The Acceleration of Electrons by Magnetic Induction.. Phys. Rev., 60, 47-53  
 2451 (1941)
- 2452 6. SATURNEI photos: FAR\_SA\_N\_00248, FAR\_SA\_N\_02826; credit CEA Saclay. Archives  
 2453 historiques CEA. Copyright CEA/Service de documentation
- 2454 7. Sessler, A., Wilson, E.: Engines of Discovery. A Century of Particle Accelerators. World  
 2455 Scientific, 2007
- 2456 8. Fig. 9.3: Credit Reider Hahn, Fermilab
- 2457 9. Endo, K., et al.: Compact proton and carbon ion synchrotrons for radiation therapy. MOPRI087,  
 2458 Proceedings of EPAC 2002, Paris, France; pp. 2733-2735.  
 2459 <https://accelconf.web.cern.ch/e02/PAPERS/MOPRI087.pdf>
- 2460 10. Vostrikov, V.A., et al.: Novel approach to design of the compact proton synchrotron magnetic  
 2461 lattice. tupsa17, 26th Russian Particle Accelerator Conference RUPAC2018, Protvino, Russia  
 2462 (2018).  
 2463 <https://accelconf.web.cern.ch/rupac2018/papers/tupsa17.pdf>
- 2464 11. Cohen, D., : Feasibility of Accelerating Polarized Protons with the Argonne ZGS. Review of  
 2465 Scientific Instruments 33, 161 (1962).// <https://doi.org/10.1063/1.1746524>
- 2466 12. Ratner, L.G. and Khoe, T.K.: Acceleration of Polarized Protons in the Zero Gradient Syn-  
 2467 chrotron. Procs. PAC 1973 Conference, Washington (1973).  
 2468 [http://accelconf.web.cern.ch/p73/PDF/PAC1973\\_0217.PDF](http://accelconf.web.cern.ch/p73/PDF/PAC1973_0217.PDF)
- 2469 13. Bywatwr, J., Khoe, T., et al.: A pulsed quadrupole system for preventing depolarization. IEEE  
 2470 Transactions on Nuclear Science (Volume: 20, Issue: 3, June 1973)
- 2471 14. Cho, Y., et als.: Effects of depolarizing resonances on a circulating beam of polarized protons  
 2472 during or storage in a synchrotron. IEEE Trans. Nuclear Science, Vol.NS-24, No.3, June 1977
- 2473 15. Parker, E.F.: High Energy Polarized Deuterons at the Argonne National Laboratory Zero  
 2474 Gradient Synchrotron. IEEE Transactions on Nuclear Science, Vol. NS-26, No. 3, June 1979,  
 2475 pp 3200-3202

- 2476 16. Leleux, G.: Accélérateurs Circulaires. Lecture Notes, INSTN, CEA Saclay (1978)
- 2477 17. Suddeth, D.E., et als.: Pole face winding equipment for eddy current correction at the Zero
- 2478 Gradient Synchrotron. Procs. PAC 1973 Conference, Washington (1973).
- 2479 [http://accelconf.web.cern.ch/p73/PDF/PAC1973\\_0397.PDF](http://accelconf.web.cern.ch/p73/PDF/PAC1973_0397.PDF)
- 2480 18. Raugas, A.V. and Wright, A.J.: Betatron tune profile control in the Zero Gradient Synchrotron
- 2481 (ZGS) using the main magnet pole face windings. Procs. PAC1977 conference, IEEE Trans.
- 2482 on Nucl. Science, VoLNS-24, No.3, June 1977
- 2483 19. Floquet, G.: Sur les équations différentielles linéaires à coefficients périodiques. Annales
- 2484 scientifiques de l'E.N.S. 2e série, tome 12 (1883), p. 47-88.
- 2485 [http://www.numdam.org/item?id=ASENS\\_1883\\_2\\_12\\_\\_47\\_0](http://www.numdam.org/item?id=ASENS_1883_2_12__47_0)
- 2486 20. Leleux, G.: Traversée des résonances de dépolarisation. Rapport Interne LNS/GT-91-15,
- 2487 SATURNE, Groupe Théorie, CEA Saclay (février 1991)
- 2488 21. Méot, F.: Spin Dynamics. Polarized Beam Dynamics and Instrumentation in Particle Accel-
- 2489 erators, USPAS Summer 2021 Spin Class proceedings, Springer (2023)
- 2490 22. Lee, S.Y.: Spin Dynamics and Snakes in Synchrotrons. World Scientific, 1997
- 2491 23. Khoe, T.K., et al.: The High Energy Polarized Beam at the ZGS. Procs. IXth Int. Conf on
- 2492 High Energy Accelerators, Dubna, pp. 288-294 (1974).
- 2493 Fig. 9.16: Copyrights under license CC-BY-3.0, <https://creativecommons.org/licenses/by/3.0/>;
- 2494 no change to the material
- 2495 24. Froissart, M. and Stora, R.: Dépolarisation d'un faisceau de protons polarisés dans un syn-
- 2496 chrotron. Nucl. Inst. Meth. 7 (1960) 297.
- 2497 25. Bruck H., Debraine P., Levy-Mandel R., Lutz J., Podliasky I., Prevot F., Taieb J., Winter S.D.,
- 2498 Maillet R., Caractéristiques principales du Synchrotron à Protons de Saclay et résultats obtenus
- 2499 lors de la mise en route, rapport CEA no.93, CEN-Saclay, 1958.
- 2500 26. Méot, F.: Zgoubi Users' Guide.
- 2501 <https://www.osti.gov/biblio/1062013-zgoubi-users-guide> Sourceforge latest version:
- 2502 <https://sourceforge.net/p/zgoubi/code/HEAD/tree/trunk/guide/Zgoubi.pdf>
- 2503 27. Foss, M.H., et al.: The Argonne ZGS Magnet. IEEE 1965, pp. 377-382, June 1965
- 2504 28. Klaisner, L.A., et al.: IEEE 1965, pp. 133-137, June 1965